PHYSICAL REVIEW B **93**, 235204 (2016)

Realistic multiband $k \cdot p$ approach from *ab initio* and spin-orbit coupling effects of InAs and InP in wurtzite phase

Paulo E. Faria Junior,[1,*] Tiago Campos,[1,2] Carlos M. O. Bastos,[1] Martin Gmitra,[2] Jaroslav Fabian,[2] and Guilherme M. Sipahi[1,3]
[1]*São Carlos Institute of Physics, University of São Paulo, 13566-590 São Carlos, São Paulo, Brazil*
[2]*Institute for Theoretical Physics, University of Regensburg, 93040 Regensburg, Germany*
[3]*Department of Physics, State University of New York at Buffalo, Buffalo, New York 14260, USA*
(Received 20 April 2016; published 30 June 2016)

Semiconductor nanowires based on non-nitride III-V compounds can be synthesized under certain growth conditions to favor the appearance of the wurtzite crystal phase. Despite reports in the literature of *ab initio* band structures for these wurtzite compounds, we still lack effective multiband models and parameter sets that can be simply used to investigate physical properties of such systems, for instance, under quantum confinement effects. In order to address this deficiency, in this study we calculate the *ab initio* band structure of bulk InAs and InP in the wurtzite phase and develop an 8×8 $k \cdot p$ Hamiltonian to describe the energy bands around the Γ point. We show that our $k \cdot p$ model is robust and can be fitted to describe the important features of the *ab initio* band structure. The correct description of the spin-splitting effects that arise due to the lack of inversion symmetry in wurtzite crystals is obtained with the k-dependent spin-orbit term in the Hamiltonian, often neglected in the literature. All the energy bands display a Rashba-like spin texture for the in-plane spin expectation value. We also provide the density of states and the carrier density as functions of the Fermi energy. Alternatively, we show an analytical description of the conduction band, valid close to the Γ point. The same fitting procedure is applied to the 6×6 valence band Hamiltonian. However, we find that the most reliable approach is the 8×8 $k \cdot p$ Hamiltonian for both compounds. The $k \cdot p$ Hamiltonians and parameter sets that we develop in this paper provide a reliable theoretical framework that can be easily applied to investigate electronic, transport, optical, and spin properties of InAs- and InP-based nanostructures.

DOI: 10.1103/PhysRevB.93.235204

I. INTRODUCTION

In the past decade, the development of low-dimensional III-V semiconductor nanostructures has witnessed great advances [1]. For instance, one interesting feature that was observed in the synthesis of III-V nanowires is the appearance of the wurtzite (WZ) crystal phase, instead of the usual zinc-blende (ZB) [2]. This created new possibilities of III-V compounds with WZ structure besides the well-established nitride-based materials. Moreover, controlling the growth conditions, e.g., temperature and III/V ratio, it is possible to achieve not only single crystal phase nanowires [3,4] but also to mix ZB and WZ regions with sharp interfaces in the same nanostructure, which is known as polytypism [5–7]. It has been demonstrated that mixed phases greatly affect the physical properties, for example, of the light polarization [8–10], electron transport [11,12], and photoconductivity [13].

Among these new III-V compounds with WZ structure, InAs and InP are particularly important. InAs WZ has a large spin-orbit coupling (SOC) which favors the study of spin-related phenomena, for instance, spin field effect transistors [14], and the search for the elusive Majorana fermions [15]. Also, InAs WZ shows remarkable piezoelectric and piezoresistive properties [16] that, combined with the InAs narrow band gap, can operate in the near-infrared regime. On the other hand, InP is a promising candidate for photovoltaic applications [17] and for enhancing the efficiency of solar cells [18]. In fact, a silicon-integrated nanolaser of InP nanowire has already been demonstrated at room temperature with a wide wavelength range due to the WZ/ZB polytypism [19]. Furthermore, it is also possible to combine InAs and InP WZ compounds in axial [20] and radial [21] heterostructures, which opens the path for novel opportunities in band gap engineering.

Theoretical studies based on WZ III-V compounds including InAs and InP were reported using different *ab initio* approaches. The main focus of these studies was the determination of the lattice parameters, band gaps, and SOC energy splittings in the valence band [22–27]. Of these references, De and Pryor [23] provide useful information that can be used in effective models, such as the effective masses and the spin-splitting parameters. The issue of using these parameters is that they are only valid in the immediate vicinity of the Γ point [$\sim$2% of the first Brillouin zone (FBZ)], limiting the range of physical phenomena that can be investigated. In order to achieve a better description farther away from the Γ point, a multiband effective model is desirable. Although $k \cdot p$ models and parameters are well established for WZ III-nitride compounds [28,29], there are only a few reports in the literature for non-nitrides, such as InP [10,30] and GaAs [31].

In this study, we develop a robust 8×8 $k \cdot p$ Hamiltonian to describe the *ab initio* band structure calculated by WIEN2k [32] of InAs and InP in the WZ phase. We show that our fitted parameters reproduce the *ab initio* band structure, capturing the important anticrossings and spin-splitting features up to 1.0 nm^{-1} ($\sim$10% of the FBZ in the $k_x k_y$ plane and $\sim$22% in the k_z direction). At Γ point, each band is twofold degenerate and for the valence band we found that the band ordering, from top to bottom, is HH (heavy hole), CH

---

[*] fariajunior.pe@gmail.com

(crystal field split-off hole), and LH (light hole) for InAs and HH, LH, and CH for InP. This ordering is due to an interplay of SOC energy splittings and the crystal field energy splitting. The intricate behavior of spin splittings, arising from the bulk inversion asymmetry (BIA) of the WZ structure, is correctly described by the k-dependent SOC term, often neglected in the literature. Calculating the spin expectation value for the Bloch states, we find a Rashba-like spin texture [33] with either clockwise (CW) or counterclockwise (CCW) orientation. All these spin-dependent features extracted from our $k \cdot p$ Hamiltonian and parameter sets were systematically checked to agree with *ab initio* calculations. Furthermore, based on our effective 8×8 Hamiltonian, we calculated the density of states (DOS) and predict the carrier density as a function of the Fermi energy. We also provide an analytical description of the conduction band valid close to the Γ point and a compact description of the valence band (6×6 Hamiltonian). But, we would like to emphasize that the best description of InAs and InP WZ is obtained using the total 8×8 Hamiltonian. In summary, the main goal of our paper is to provide a realistic $k \cdot p$ description that can be used to study charge and spin transport, optics, as well as (superconducting) proximity effects in semiconductor heterostructures, e.g., quantum wells and wires. Such heterostructures cannot be investigated by first principles due to their mesoscopic sizes, and the $k \cdot p$ technique (using the prescription $\vec{k} \rightarrow -i\vec{\nabla}$) is currently perhaps the best choice for obtaining physically relevant quantities for them.

This paper is organized as follows: In Sec. II we present the *ab initio* band structure of InAs and InP WZ. The multiband $k \cdot p$ model and its considerations are discussed in Sec. III. In Sec. IV, we describe our main results: (i) the fitting approach, (ii) the comparison between the *ab initio* and $k \cdot p$ for band structure and the spin splittings, (iii) the spin expectation value for all energy bands, and (iv) the DOS extracted from the 8×8 Hamiltonian. The analytical description of the conduction band (CB) close to the Γ point is presented in Sec. V, and the compact form of the valence Hamiltonian, along with its parameters, is shown in Sec. VI. Finally, in Sec. VII we present our conclusions and possible direct applications of our effective multiband model.

II. *AB INITIO* BAND STRUCTURE

The *ab initio* electronic structure for InAs and InP in the WZ phase was calculated within the density functional theory (DFT) framework [34], using the full potential linearized augmented plane wave method implemented by the WIEN2k code [32]. To account for local and semilocal functional deficiencies to correctly describe band gaps in semiconductors, we used an efficient and accurate alternative for electronic structure calculations based on the modified Becke-Johnson (mBJ) exchange potential [35] with LDA (local density approximation) correlation [36]. It has been shown that the semilocal mBJ exchange potential provides prediction of band gaps of the same order [37–39] as hybrid functionals [40] and the *GW* method [41–43]. In addition, the semilocal approach to the exchange-correlation functional is barely expensive when compared to the LDA [44] or the generalized gradient approximation [45]. The SOC is included within the second variational step [46]. Regarding the technical details of our calculations, we expanded the wave functions in atomic spheres for orbital quantum numbers up to 10; the plane wave cutoff multiplied with the smallest atomic radii equals 10 and the irreducible Brillouin zone was sampled with 600 k points. Further details on *ab initio* calculations of III-V semiconductors, either with ZB or WZ structure, using the mBJ potential can be found in Ref. [47].

The particular order of cation (In) and anions (As, P) within the unit cell determines spin orientation [49]. We consider the following primitive basis vectors for corresponding hexagonal Bravais lattice, $\vec{a}_1 = a(\sqrt{3}, -1,0)/2$, $\vec{a}_2 = a(0,1,0)$, and $\vec{a}_3 = c(0,0,1)$, where a and c are the WZ lattice parameters. Using the three basis vectors $\vec{a}_i$ $(i = 1,2,3)$ we define the following four atomic positions that form the WZ structure: $(2/3,1/3,u)$ and $(1/3,2/3,1/2 + u)$, with $u = 0$ for anion and and $u = 3/8$ for cation. We note that in general there might be $u = 3/8 + \epsilon$ with a small dimensionless cell-internal structural parameter ϵ describing a deviation from ideal tetrahedrons as one observes for SiC polytypes [50]. In our calculations we considered $\epsilon = 0$ since it is a rather small valued parameter [25,51]. For the lattice parameters we considered $a = 4.2742$ Å and $c = 7.025$ Å [52] for InAs and $a = 4.1148$ Å and $c = 6.7515$ Å [53] for InP.

We show the band structures obtained with WIEN2k in Fig. 1(a) for InAs and Fig. 1(b) for InP. Both compounds show a direct band gap at the Γ point with values of $E_g = 0.467$ eV for InAs and $E_g = 1.494$ eV for InP. Due to the hexagonal

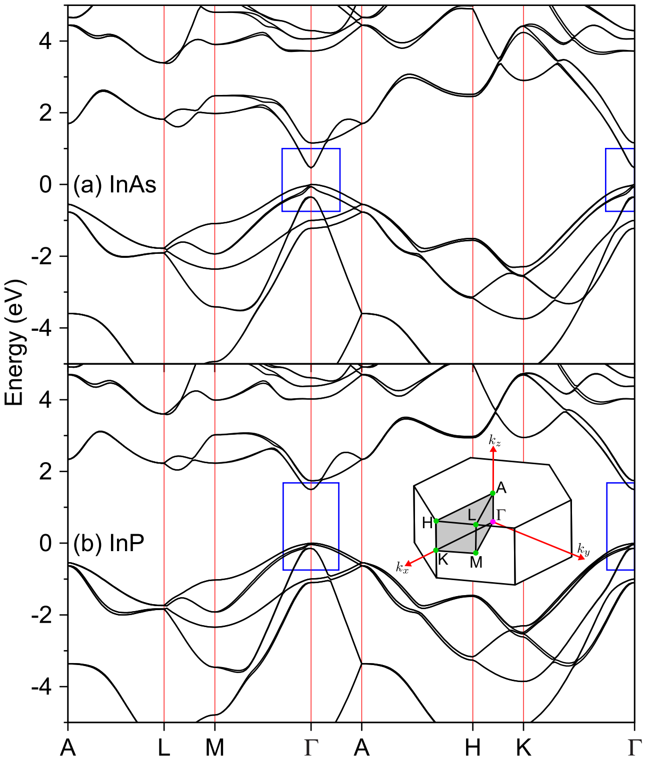

FIG. 1. *Ab initio* band structure along high-symmetry lines for (a) InAs and (b) InP in WZ phase. The inset shows the FBZ of WZ structure indicating the high-symmetry points. The rectangles highlight the region of interest around the Γ point.

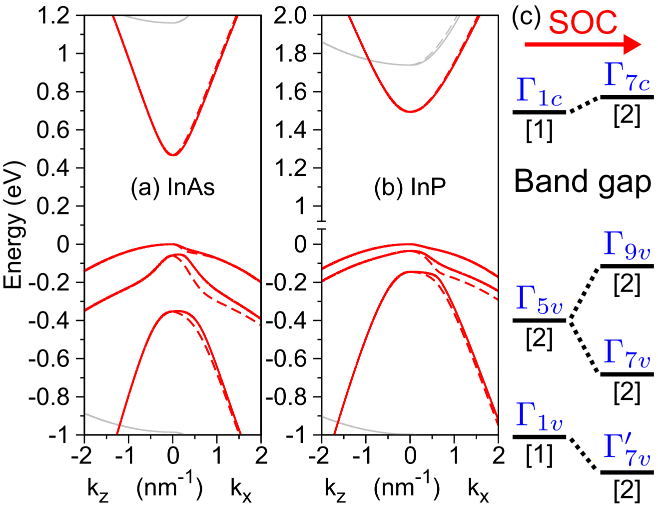

FIG. 2. Band structure for WZ (a) InAs and (b) InP around Γ point for k_z (Γ-A) and k_x (Γ-K) directions. The solid lines indicate the outer branch and the dashed lines indicate the inner branch of the spin-split bands. The thin (gray) lines indicate the energy bands outside our range of interest. (c) Change in the irreducible representations of energy bands at Γ point under SOC. The subscripts v and c added to the irreducible representations indicate valence and conduction bands, respectively, and the prime distinguishes between the two possibilities of Γ_7. The numbers in square brackets are the degeneracy of the bands. Our notation for the irreducible representations follows Ref. [48].

symmetry of WZ, the Γ point, as well as the symmetry line connecting Γ-A (hexagonal axis), belongs to the C_{6v} symmetry group [54], which has only two-dimensional double-group representations. From this follows that the states along the hexagonal axis are spin degenerate [54,55]. Irreducible representations of other points in the FBZ compatible with spin are singly degenerate. Hence, except for accidental or time-reversal degeneracies at Γ and A points, spin splittings must occur for all bands.

In Figs. 2(a), for InAs, and 2(b), for InP, we display the rectangular regions of Fig. 1, i.e., a zoom of the band structure around the Γ point. At this energy range, the anticrossing and spin-splitting features of the band structures are evident. Because of large SOC in InAs, the valence band energy levels are farther apart than InP bands and additional curvatures are present along the k_z direction. For InP the top two valence bands along k_z show similar curvatures and no anticrossing is visible. The effect of SOC in the energy bands at the Γ point is shown schematically in Fig. 2(c). Without SOC, the irreducible representations belong to the simple group, while with SOC, they are referred to as the double group. This distinction is important for $k \cdot p$ perturbative approaches.

We present a comparison between our *ab initio* calculations and other theoretical papers in the literature in Table I. Besides the lattice constants a and c we compare the values of the internal parameter u, the energy gap E_g, and the energy difference between the top valence band Γ_{9v} and the other bands Γ_{7v} and Γ'_{7v} [following the notation of Fig. 2(c)]. These energy differences are defined as $\Delta E_{97} = E(\Gamma_{9v}) - E(\Gamma_{7v})$ and $\Delta E'_{97} = E(\Gamma_{9v}) - E(\Gamma'_{7v})$. It is very common to compare the crystal field splitting energy, Δ_1, and the SOC energy, Δ_{SO}; however, these parameters are usually obtained under the quasicubic approximation and do not provide a direct comparison with experiments such as ΔE_{97} and $\Delta E_{97'}$. We can see that all the values obtained by our calculations are within the range of reported data in previous papers. We also compare experimental measurements of the energy gap with our calculated values, shown in Table II. We focused on experimental data obtained by photoluminescence measurements at low temperature of large-diameter nanowires, so that lateral quantum confinement is negligible. For both InAs (despite the reduced set of available data) and InP compounds, our calculated values of the energy gaps are consistent with the experiments. Furthermore, photoluminescence excitation measurements can probe the Γ_{7v} and Γ'_{7v} valence bands and allow us to check our calculated values for ΔE_{97} and $\Delta E'_{97}$ energies. To the best of our knowledge, such experiments are only available for InP. Typical values found for ΔE_{97} and $\Delta E'_{97}$ in InP WZ are 0.044 eV and 0.187 eV in Ref. [9], 0.043 eV and 0.179 eV in Ref. [56], and 0.044 eV and 0.182 eV in Ref. [57]. Our calculated values for InP of $\Delta E_{97} = 0.0354$ eV and

TABLE I. Comparison of theoretical data for InAs and InP in WZ phase. The lattice constants a and c are given in Å, and u is dimensionless. The band gap, E_g, and the valence band energy differences, ΔE_{97} and $\Delta E'_{97}$, are given in eV.

		a	c	u	E_g	ΔE_{97}	$\Delta E'_{97}$
InAs	This study	4.2742	7.0250	0.37500	0.4670	0.0592	0.3527
	Ref. [23]	4.1505	6.7777	0.37500	0.4810	0.1050	0.4690
	Ref. [25]*	4.2570	6.9894	0.37447	0.4810	0.0573	0.3937
	Ref. [27]	4.2564	7.0046	0.37400	0.4610	0.0700	0.3640
	Ref. [47]	4.2742	7.0250	0.37422	0.4610	0.0660	0.3600
InP	This study	4.1148	6.7515	0.37500	1.4940	0.0354	0.1450
	Ref. [23]	4.2839	6.9955	0.37500	1.4740	0.0630	0.3480
	Ref. [24]	4.1500	6.9120	0.37100	1.4936	0.0450	0.2430
	Ref. [25][a]	4.1148	6.7515	0.37458	1.5760	0.0321	0.1339

[a] The values of a, c, and u are from Ref. [53].

TABLE II. Comparison between theoretical and experimental values of the energy gap. We indicate the temperature of the photoluminescence measurements in parentheses.

	E_g (eV) This study	E_g (eV) Experiment
InAs	0.467	0.520 (7 K)[a], 0.500 (20 K)[b] 0.458 (5 K)[c]
InP	1.494	1.492 (10 K)[d], 1.494 (10 K)[e] 1.490 (20 K)[f], 1.491 (4 K)[g] 1.493 (4 K)[h], 1.488 (6 K)[i]

[a] Reference [60]
[b] Reference [61]
[c] Reference [62]
[d] Reference [57]
[e] Reference [56]
[f] Reference [63]
[g] Reference [3]
[h] Reference [64]
[i] Reference [9].

$\Delta E'_{97} = 0.145$ eV (from Table I) are also in good agreement with these experimental trends. For completeness, we provide in Appendix A the calculated values of effective masses around the Γ point.

III. $k \cdot p$ FORMULATION

One alternative approach to *ab initio* band structure calculations is the $k \cdot p$ method. In the $k \cdot p$ approach, the many-body interactions of electrons with nuclei and other electrons are described by an effective potential which has the same periodicity as the Bravais lattice of the crystal [58]. Such periodic property of the potential allows us to use Bloch's theorem for the total wave function. The single-particle Hamiltonian for the periodic part of the Bloch function, $u_{n,\vec{k}}(\vec{r})$, can be written as

$$\mathbf{H} = \underbrace{\frac{p^2}{2m_0} + V(\vec{r})}_{\mathbf{H_0}} + \underbrace{\frac{\hbar}{4m_0^2c^2}[\vec{\nabla}V(\vec{r}) \times \vec{p}] \cdot \vec{\sigma}}_{\mathbf{H_{SO}}} + \underbrace{\frac{\hbar^2k^2}{2m_0}}_{\mathbf{H_{k2}}} + \underbrace{\frac{\hbar}{m_0}\vec{k} \cdot \vec{p}}_{\mathbf{H_{kp}}} + \underbrace{\frac{\hbar^2}{4m_0^2c^2}[\vec{\nabla}V(\vec{r}) \times \vec{k}] \cdot \vec{\sigma}}_{\mathbf{H_{kSO}}}, \tag{1}$$

in which the different terms in the Hamiltonian are identified for convenience.

We can solve the above equation perturbatively expanding the functions $u_{n,\vec{k}}(\vec{r})$ around a specific reciprocal space point for which we know the solutions for the Hamiltonian. Since WZ InAs and InP have a direct band gap at the Γ point, this is the chosen expansion point. The perturbative technique we use in this paper is Löwdin's formalism [59]. In this approach, the functions at the Γ point, i.e., the basis set to expand $u_{n,\vec{k}}(\vec{r})$, are divided into classes A and B. The energy bands we are interested in describing comprise the class A while the other energy bands belong to class B. The contribution of states in class B appear in second or higher orders of perturbation. The matrix elements we consider can arise from first- or second-order perturbation, reading as

$$H^{(1)}_{f,\alpha\alpha'} = \langle\alpha|\mathbf{H_f}|\alpha'\rangle \tag{2}$$

and

$$H^{(2)}_{fg,\alpha\alpha'} = \sum_{\beta}^{B} \frac{\langle\alpha|\mathbf{H_f}|\beta\rangle\langle\beta|\mathbf{H_g}|\alpha'\rangle}{E_{\alpha\alpha'} - E_{\beta}}, \tag{3}$$

where $\mathbf{H_f}$ and $\mathbf{H_g}$ can be any of the terms of Eq. (1), except $\mathbf{H_0}$.

Since the unperturbed term, $\mathbf{H_0}$, in Eq. (1) does not contain SOC effects explicitly, we consider the simple group description of the energy bands, the most usual approach in the literature [65]. Under such approximation, the states in class A belong to the irreducible representations shown on the left side of Fig. 2(c), a 4-dimensional Hilbert space, combined with the spin-1/2 angular momentum, a 2-dimensional Hilbert space. Therefore, the 8-dimensional basis set for the $k \cdot p$ Hamiltonian in Dirac notation [66] is given by

$$\begin{array}{ll}
|c_1\rangle = -\dfrac{\left|\left(\Gamma^x_{5v} + i\Gamma^y_{5v}\right)\uparrow\right\rangle}{\sqrt{2}}, & |c_5\rangle = -\dfrac{\left|\left(\Gamma^x_{5v} + i\Gamma^y_{5v}\right)\downarrow\right\rangle}{\sqrt{2}}, \\
|c_2\rangle = \dfrac{\left|\left(\Gamma^x_{5v} - i\Gamma^y_{5v}\right)\uparrow\right\rangle}{\sqrt{2}}, & |c_6\rangle = |\Gamma_{1v}\downarrow\rangle, \\
|c_3\rangle = |\Gamma_{1v}\uparrow\rangle, & |c_7\rangle = i|\Gamma_{1c}\uparrow\rangle, \\
|c_4\rangle = \dfrac{\left|\left(\Gamma^x_{5v} - i\Gamma^y_{5v}\right)\downarrow\right\rangle}{\sqrt{2}}, & |c_8\rangle = i|\Gamma_{1c}\downarrow\rangle,
\end{array} \tag{4}$$

with 1–6 representing the valence band states and 7–8 the conduction band states. Since Γ_{5v} is two dimensional, we identified its basis states by $|\Gamma^x_{5v}\rangle \sim x$ and $|\Gamma^y_{5v}\rangle \sim y$. The single arrows $(\uparrow,\downarrow)$ represent the projection of spin up and spin down, eigenvalues of the σ_z Pauli matrix. The states in class B have simple group symmetries Γ_1, Γ_3, Γ_5, and Γ_6, which is the only necessary information to calculate second-order contributions.

To describe the interaction among the energy bands, we consider all terms of Eq. (1) in first-order perturbation and only the term $\mathbf{H_{kp}}$ in second order. Therefore, the total matrix Hamiltonian in the basis set (4) comprises the following terms:

$$H = H_0 + H^{(1)}_{SO} + H^{(1)}_{kp} + H^{(1)}_{kSO} + H^{(2)}_{kp}, \tag{5}$$

with the explicit form of each matrix and the definition of the parameters given in Appendix B.

In Fig. 3 we show schematically the interactions for each term in the total Hamiltonian (5). The Fig. 3(a) represents the unperturbed Hamiltonian without SOC, where states $|c_{1(4)}\rangle$ and $|c_{2(5)}\rangle$ are degenerate for spin up (down). The only terms that couple different spin projections arise from $H^{(1)}_{SO}$ or $H^{(1)}_{kSO}$, Figs. 3(b) and 3(d), respectively. Usually $H^{(1)}_{kSO}$ is neglected in WZ Hamiltonians [28,29,31,67–70]. However, the explicit interactions for nonzero k values are crucial to correctly describe the spin-splitting properties. We included $H^{(1)}_{kSO}$ following the approach of Dresselhaus for ZB [71]. Moreover, the coupling of $H^{(1)}_{SO}$ to other terms provides additional contributions to the spin splitting of energy bands. Besides spin-splitting properties, we want a good description of the band structure curvatures. Such effects can be modeled by linear and quadratic terms of the $H^{(1)}_{kp}$ and $H^{(2)}_{kp}$, Figs. 3(c) and 3(e), respectively. The only term that allows a k-dependent self-interaction of states is $H^{(2)}_{kp}$ which gives the effective mass contribution to our model.

Although the $k \cdot p$ method provides the functional form of the Hamiltonian, the parameters that describe different materials cannot be found by group theory arguments only. In order to calculate the matrix elements we would need the functions at the expansion point and also the periodic potential $V(\vec{r})$. Alternatively, we can directly fit the $k \cdot p$ Hamiltonian to the *ab initio* band structure to extract the parameters [29,31,67,69,72].

IV. NUMERICAL FITTING OF THE 8 × 8 $k \cdot p$ HAMILTONIAN

We start our fitting approach by calculating the k-independent parameters of the Hamiltonian, i.e., the energy

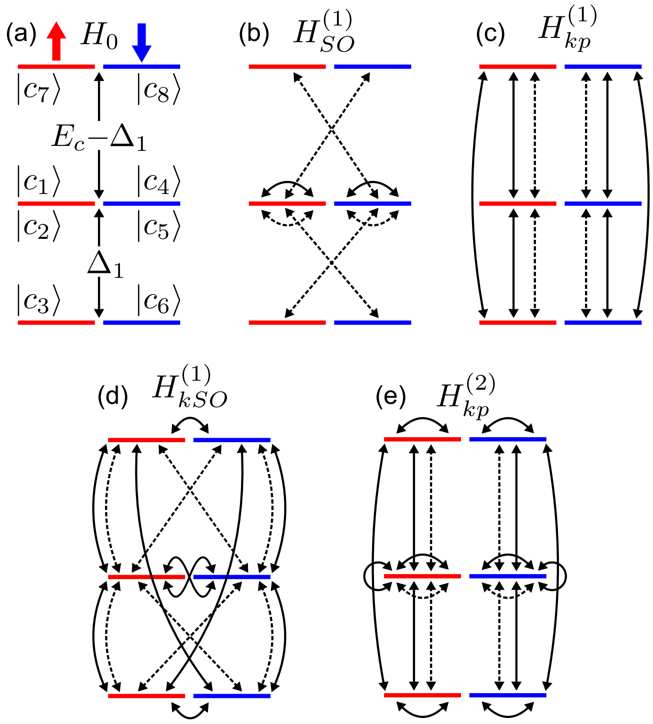

FIG. 3. Possible interactions of the Hamiltonian terms (a) H_0, (b) $H_{SO}^{(1)}$, (c) $H_{kp}^{(1)}$, (d) $H_{kSO}^{(1)}$, and (e) $H_{kp}^{(2)}$. The arrows on top of panel (a) indicate spin-up and spin-down projections of the basis states. Since $|c_{1(4)}\rangle$ and $|c_{2(5)}\rangle$ are degenerate, we indicate the interactions arising from $|c_{1(4)}\rangle$ with solid lines and the interactions arising from $|c_{2(5)}\rangle$ with dashed lines. For the other states without degeneracy we used solid lines. In panel (a) we show the energy splittings without SOC, formally defined in Appendix B.

splittings. The values for crystal field splitting, Δ_1, and the conduction band energy, E_c, can be obtained from the *ab initio* calculation without SOC, which is in fact the assumption of the $k \cdot p$ perturbative theory [H_0 term; see Fig. 3(a)]. This approach is very useful because it simplifies the calculation of the SOC energy splittings inside the valence band, Δ_2 (coupling same spins) and Δ_3 (coupling different spins), and the SOC between conduction and valence bands, Δ_4. Please refer to Appendix B for the formal definition of these splitting energies. By setting the values of Δ_1 and E_c, it possible to have $\Delta_2 \neq \Delta_3$ and neglect the cubic approximation [28]. If the values of Δ_1 and E_c were not found without SOC, we would have to determine 5 variables having only 3 linear independent combinations of the energy bands with SOC. This approach would provide a range of possible values and further analysis would be necessary. Starting with Δ_1 and E_c values without SOC, we obtained four different solution sets for the SOC splitting energies since Δ_3 and Δ_4 are off-diagonal terms in the Hamiltonian and can assume positive or negative values with the same magnitude. At the Γ point any of these solution sets give the same eigenvalues; therefore we set Δ_3 to be positive [23–25,27] and investigated the effect of positive and negative values of Δ_4.

Before starting the fitting of the k-dependent parameters, it is important to define the fitting region we are interested in, which is connected to the limits of our $k \cdot p$ model. Basically, in order to describe as precisely as possible the 8 bands we are interested in, we should stay in a region away from the influence of remote bands, roughly $k \sim 1.5$ nm^{-1}; see Figs. 2(a) and 2(b). We also want to have a nice description of the anticrossings in the band structure around $k \sim 0.5$ nm^{-1}. Furthermore, in the $k \cdot p$ Hamiltonian k_x and k_y directions are equivalent, but this is not the case for the *ab initio* band structure. Around $k \sim 1.0$ nm^{-1}, the *ab initio* band structures along the Γ-K and Γ-M directions are different, especially the spin splitting, which is another feature to be described. Therefore, it is reasonable to set the goal of our fitting at $k = 1.0$ nm^{-1} to find the best parameter set that describes the *ab initio* band structure around the Γ point for all 8 bands.

To increase the accuracy of our parameter sets, we fitted, simultaneously, the energy bands in multiple directions of the FBZ (Γ-K, Γ-M, Γ-A, Γ-H, and Γ-L). The fitting algorithm was developed using the LMFIT [73] package of Python assuming several minimization methods available. We noticed that the minimization methods behave differently and usually provide different parameter sets. After an initial fit, we chose the best parameter set and used it as input for a new fit using all minimization methods again. To find the best fit, the band structures and spin splittings are compared by their residue [74] up to $k = 1.0$ nm^{-1} for all directions. The best parameter sets for InAs and InP found by our fitting approach are presented in Table III.

TABLE III. Parameter sets of the 8 × 8 Hamiltonian for InAs and InP WZ. The energy splittings are given in eV, linear parameters in eV Å, and second-order parameters in units of $\hbar^2/2m_0$.

Parameter	InAs	InP
Energy splittings		
Δ_1	0.1003	0.0945
Δ_2	0.1023	0.0279
Δ_3	0.1041	0.0314
Δ_4	0.0388	0.0411
E_c	0.6649	1.6142
Linear parameters		
A_7	−0.4904	−0.1539
P_1	8.3860	7.6349
P_2	6.8987	5.5651
α_1	−0.0189	0.2466
α_2	−0.2892	−0.2223
α_3	−0.5117	−0.2394
β_1	−0.0695	−0.0481
β_2	−0.2171	−0.1386
γ_1	0.5306	0.2485
Second order parameters		
A_1	1.5726	−1.0419
A_2	−1.6521	−0.9645
A_3	−2.6301	−0.0694
A_4	0.5126	−1.2760
A_5	0.1172	−1.1024
A_6	1.3103	−0.5677
e_1	−3.2005	−0.5732
e_2	0.6363	2.4084
B_1	−2.3925	−7.7892
B_2	2.3155	4.3981
B_3	−1.7231	9.1120

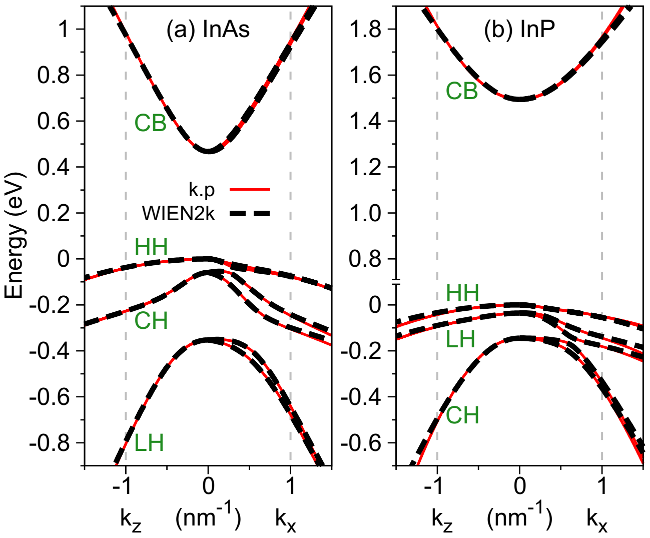

FIG. 4. Comparison of band structures calculated from the fitted $k \cdot p$ model (solid lines) and the *ab initio* WIEN2k (dashed lines) for (a) InAs and (b) InP. The vertical dashed lines at 1.0 nm^{-1} indicate the borders of the fitting range.

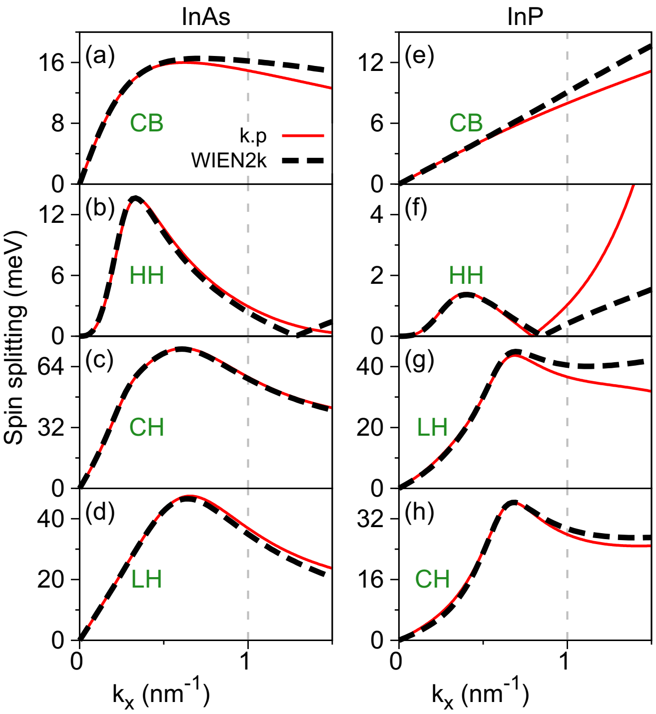

FIG. 5. Comparison of the spin splittings along k_x for the energy bands (a) CB, (b) HH, (c) CH, and (d) LH of InAs and (e) CB, (f) HH, (g) LH, and (h) CH of InP. The line schemes follow Fig. 4.

In Fig. 4, we present the comparison between the fitted and WIEN2k *ab initio* band structures along k_z and k_x for InAs and InP. All the important features around the Γ point, i.e., anticrossings and spin splittings, are captured by our model. We notice a good agreement up to $k = 1.0\ \text{nm}^{-1}$ with small deviations above it, indicating that we are reaching the region where the influence of remote energy bands becomes important. We labeled the valence bands according to the composition of states at the Γ point. Following Chuang and Chang's notation [75], HH is purely composed of $|c_{1(4)}\rangle$ states, LH has more contribution from $|c_{2(5)}\rangle$ than $|c_{3(6)}\rangle$ states, and CH has more contribution from $|c_{3(6)}\rangle$ than $|c_{2(5)}\rangle$ states. Since this analysis is usually performed without the Δ_4 parameter, we also calculated Δ_2 and Δ_3 considering $\Delta_4 = 0$ and we found that the same labeling holds (these values are shown in Sec. VI). Furthermore, we also compared the $k \cdot p$ composition with the projection to atomic orbitals of the *ab initio* wave functions and the same trends can be noticed. The labeling order of CH-LH in InAs is due to the values of SOC splitting energies, which are slightly larger than the crystal field splitting. For InP, the crystal field splitting is dominant leading to LH-CH ordering. Although this labeling of the valence band can be confusing, it is very useful to extract optical trends from the band-egde transitions. For instance, if we take into account optical transitions arising from the top two valence bands, we can expect InP light polarization to be more in-plane due to LH contribution than InAs due to CH contribution. Finally, for the conduction band of both InAs and InP we simply label it CB, short notation for conduction band; CB is mainly composed of $|c_{7(8)}\rangle$ states.

Let us take a closer look at the spin-splitting properties obtained from the $k \cdot p$ model and the *ab initio*. We show the comparison between the two methods in Fig. 5 for InAs and InP along the k_x direction. Similarly to the band structure, we have a good agreement up to $k = 1.0\ \text{nm}^{-1}$ with deviations above this region. The intricate behaviors, i.e., the appearance of maxima and crossings between HH spin-split bands, are also described by our model. All these spin-splitting characteristics have only one physical origin, the BIA of the WZ structure. The strength of SOC is greater in InAs than InP, visible at the peak values and positions. From the largest to the smallest values of the spin splitting, we have CH (LH), LH (CH), CB, and HH for InAs (InP). Furthermore, a linear behavior is maintained for InP CB throughout the fitting region. For InAs, this linear behavior is attained only in a small region close to the Γ point. In Appendix C, we present the band structure and spin splittings for the other FBZ directions used in the fitting.

Another feature we investigated is the spin orientation, i.e., the spin expectation value, $\langle\vec{\sigma}\rangle$, for the different energy bands, presented in Fig. 6 for the $k_x k_y$ plane ($k_z = 0$). We chose the constant-energy contours to be $E_n(k_x = 0.5\ \text{nm}^{-1}, k_y = 0, k_z = 0)$ of the outer branch, i.e., $E_{\text{CB}} \sim 630.0$ meV, $E_{\text{HH}} \sim -37.2$ meV, $E_{\text{CH}} \sim -123.0$ meV, $E_{\text{LH}} \sim -391.8$ meV for InAs and $E_{\text{CB}} \sim 1563.5$ meV, $E_{\text{HH}} \sim -21.9$ meV, $E_{\text{LH}} \sim -75.0$ meV, $E_{\text{CH}} \sim -156.7$ meV for InP. We found that all the investigated energy bands show a Rashba-like spin texture. For InAs, the bands CB, HH, and CH have the same spin texture, i.e., CW (CCW) orientation for the inner (outer) branch, while LH has the CCW (CW) orientation for the inner (outer) branch. In other words, the top two valence bands have the same spin texture while the third valence band has the opposite. For InP, the same spin texture holds, even though the labeling of CH and LH is reversed. The spin textures calculated with the $k \cdot p$ model were also checked with the *ab initio* calculations.

Performing the fitting approach with the negative sign of Δ_4 we obtained the same behavior of the band structure and the spin splittings, but with a reversed orientation in the spin texture, i.e., CW orientation becomes CCW and vice versa for

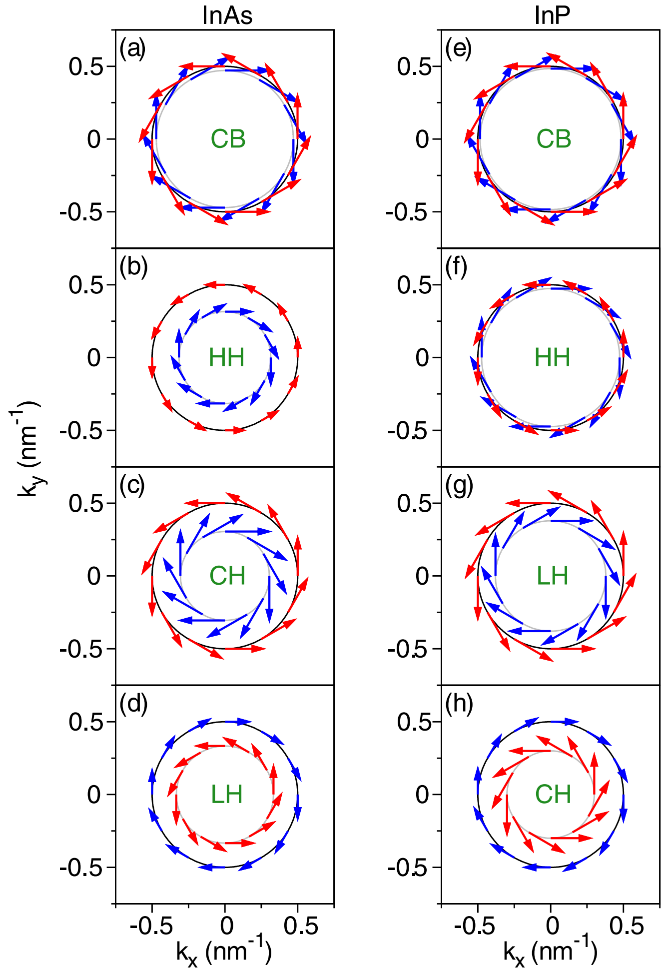

FIG. 6. Spin texture in the $k_x k_y$ plane ($k_z = 0$) for the energy bands (a) CB, (b) HH, (c) CH, and (d) LH of InAs and (e) CB, (f) HH, (g) LH, and (h) CH of InP. The blue arrows indicate clockwise orientation while the red arrows indicate counterclockwise orientation. The amplitudes of all arrows are multiplied by 0.3 to fit the figure. The constant-energy contours are also drawn in the figure in black for the outer branches and in gray for the inner branches.

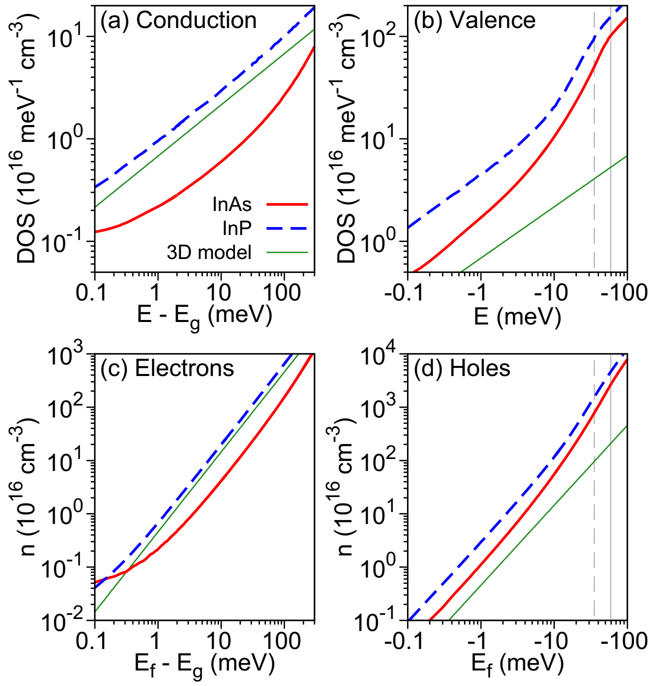

FIG. 7. Calculated DOS for (a) conduction band and (b) valence band of InAs, InP, and the 3D parabolic band model using an effective mass of $m^* = 0.1$. Carrier density, n, as a function of Fermi energy, E_f, for (c) electrons and (d) holes obtained by the integration of the DOS in panels (a) and (b), respectively. The dashed vertical lines in panels (b) and (d) indicate the LH energy at Γ point for InP while the solid vertical lines indicate the CH energy energy at Γ point for InAs.

all bands. Specifically, we found that starting with negative value of Δ_4, the signs of parameters $A_7, \alpha_1, \alpha_2, \alpha_3, \gamma_1, B_1, B_2$, and B_3 are changed, but not their amplitude. This change in the spin texture is a feature expected from *ab initio* regarding the cation and anion positions within the crystal unit cell [49] and it is reflected in our $k \cdot p$ model and parameters. Therefore, in order to provide reliable parameter sets for $k \cdot p$ Hamiltonians, not only the band structure and the spin splittings should be checked but also the spin orientation. We would like to emphasize that all these features were systematically checked in this study.

A. Density of states and carrier density

Relying on the effective 8×8 $k \cdot p$ Hamiltonian, it is straightforward to calculate a smooth DOS using a fine 3-dimensional (3D) mesh of k points ($300 \times 300 \times 300$) without much computational effort. In Fig. 7(a) we show the DOS for the conduction band of InAs and InP. For comparison, we also show the DOS for the 3D parabolic band model [DOS$(E) \propto \sqrt{E}$], which is just a straight line in the log-log scale. Due to the complex behavior of the InAs and InP conduction bands, we clearly see deviations from the linear behavior, especially for InAs. For the DOS of the valence band, presented in Fig. 7(b), the deviations from the parabolic model are much more visible, showing explicitly the need of a multiband approach. When the valence band energy approaches the CH (LH) region of InAs (InP), the DOS changes its curvature. Moreover, the valence band DOS is approximately one order of magnitude larger than the DOS of the conduction band, a behavior attributed to the small curvatures of the valence bands, i.e., large effective masses for holes (in a single band picture). Integrating the DOS we obtain the carrier density as a function of the Fermi energy, presented in Figs. 7(c) and 7(d) for electrons and holes, respectively. Typically, InP supports larger values of the carrier density than InAs. For instance, for 100 meV above the energy gap $\sim 1.6 \times 10^{18}$ cm^{-3} for InAs and $\sim 6.5 \times 10^{18}$ cm^{-3}. In the Supplemental Material [76] we provide a curve fitting of the carrier density curves that can be directly applied to predict the carrier concentration or the Fermi energy without the explicit DOS calculation using the 8×8 $k \cdot p$ Hamiltonian.

V. ANALYTICAL DESCRIPTION FOR CONDUCTION BAND

Since the conduction band has a predominant contribution of $|c_{7(8)}\rangle$ states, it is useful to provide an analytical description that holds for small regions close to the Γ point that can be easily used in spin dynamics studies. We apply Löwdin's approach again, but now dividing the basis states A [Eq. (4)] of the full matrix into two new classes A′ ($|c_{7,8}\rangle$) and B′ ($|c_{1,\cdots,6}\rangle$. Using only the terms we already calculated in the full Hamiltonian as contribution to the effective Hamiltonian, this Löwdin approach is usually referred to as folding down [59,68]. The effective Hamiltonian for the first-order folding down, keeping terms up to k^3, can be written as

$$H_{\mathrm{CB}} = M(\vec{k})\mathcal{I}_2 + \vec{\Omega}(\vec{k}) \cdot \vec{\sigma}, \tag{6}$$

in which $\mathcal{I}_2$ is a 2×2 identity matrix and M is the effective mass term given by

$$M = E_g + m_z k_z^2 + m_{xy}\left(k_x^2 + k_y^2\right), \tag{7}$$

with the coefficients m_z and m_{xy} given by

$$\begin{aligned} m_z &= e_1 + \frac{P_1^2}{E_c} + \frac{2\beta_1^2}{E_c - \Delta_1 + \Delta_2} + \frac{2\Delta_4^2(A_1 + A_3)}{(E_c - \Delta_1 + \Delta_2)^2}, \\ m_{xy} &= e_2 + \frac{1}{2}\frac{(P_2 + \beta_1)^2}{E_c - \Delta_1 + \Delta_2} + \frac{1}{2}\frac{(P_2 - \beta_1)^2}{E_c - \Delta_1 - \Delta_2} \\ &\quad + \frac{\beta_2^2}{E_c} + \frac{2\Delta_4^2(A_2 + A_4)}{(E_c - \Delta_1 + \Delta_2)^2}. \end{aligned} \tag{8}$$

The SOC field $\vec{\Omega}(\vec{k})$ is written as

$$\vec{\Omega}(\vec{k}) = \left[\alpha + \gamma_z k_z^2 + \gamma_{xy}\left(k_x^2 + k_y^2\right)\right]\begin{bmatrix} k_y \\ -k_x \\ 0 \end{bmatrix}, \tag{9}$$

with linear and cubic coefficients given by

$$\begin{aligned} \alpha &= -\gamma_1 + \frac{2\Delta_4(P_2 + \beta_1)}{E_c - \Delta_1 + \Delta_2}, \\ \gamma_z &= 2\sqrt{2}\beta_1 B_3 - \frac{2\beta_2 B_1}{E_c} + \frac{2\Delta_4(P_2 + \beta_1)(A_1 + A_3)}{(E_c - \Delta_1 + \Delta_2)^2}, \\ \gamma_{xy} &= -\frac{2\beta_2 B_2}{E_c} + \frac{2\Delta_4(P_2 + \beta_1)(A_2 + A_4)}{(E_c - \Delta_1 + \Delta_2)^2}. \end{aligned} \tag{10}$$

This analytical approach for the conduction band provides a reasonable description up to 0.2 nm^{-1} for InAs and 0.6 nm^{-1} for InP, which is roughly 100 meV above the energy gap in both cases. The numerical values of $m_z, m_{xy}, \alpha, \gamma_z$, and γ_{xy} can be obtained by replacing the parameters with values presented in Table III. Setting the k-dependent SOC parameters γ_1 and β_1 to zero, we recover the analytical linear splitting found in Ref. [68]. Our approach has the advantage of also providing the analytical description of the cubic terms. For additional corrections to the cubic term, it is possible to include higher order terms in the folding-down approach. The comparison to *ab initio* data using the analytical expressions presented in this section can be found in the Supplemental Material [76].

VI. COMPACT DESCRIPTION FOR VALENCE BAND

Because of the coupling from the crystal field and SOC energies, the best simplified description for the valence band is simply neglecting the coupling with the conduction band, thus leading to a 6×6 matrix. It is possible to write this 6×6 Hamiltonian in a compact form using direct products of 3×3 (orbital) and 2×2 (spin) matrices [28,72]. In the basis set $\{|c_1\rangle, |c_3\rangle, |c_2\rangle, |c_5\rangle, |c_6\rangle, |c_4\rangle\}$, the compact form of valence band is written as

$$\begin{aligned} H_{\mathrm{VB}} = {} & \Delta_1 J_z^2 \mathcal{I}_2 + \Delta_2 J_z \sigma_z + \sqrt{2}\Delta_3(J_+\sigma_- + J_-\sigma_+) \\ & + \left(A_1\mathcal{I}_3 + A_3 J_z^2\right)k_z^2\mathcal{I}_2 + \left(A_2\mathcal{I}_3 + A_4 J_z^2\right)\left(k_x^2 + k_y^2\right)\mathcal{I}_2 \\ & - A_5\left(J_+^2 k_-^2 + J_-^2 k_+^2\right)\mathcal{I}_2 \\ & - 2A_6 k_z(\{J_z J_+\}k_- + \{J_z, J_-\}k_+)\mathcal{I}_2 \\ & + i A_7(J_+ k_- - J_- k_+)\mathcal{I}_2 \\ & + i\sqrt{2}\alpha_1[\{J_z J_-\}(\sigma_z k_+ - 2\sigma_+ k_z) \\ & - \{J_z J_+\}(\sigma_z k_- - 2\sigma_- k_z)] \\ & + i[(\alpha_3 - \alpha_2)J_z^2 - \alpha_3\mathcal{I}_3](\sigma_+ k_- - \sigma_- k_+) \end{aligned} \tag{11}$$

with $\{J_a J_b\} = \frac{1}{2}(J_a J_b + J_b J_a)$, $J_\pm = \frac{1}{\sqrt{2}}(J_x \pm J_y)$, $\sigma_\pm = \frac{1}{2}(\sigma_x \pm \sigma_y)$, and $k_\pm = k_x \pm i k_y$. The definitions of J_x, J_y, and J_z matrices can be found in Appendix A [Eq. (A3)] of Ref. [28]. The matrix $\mathcal{I}_n$ is an n-dimensional identity. The product of 3×3 matrices (A) with 2×2 matrices (a) is defined here as

$$Aa = \begin{bmatrix} a_{11}A & a_{12}A \\ a_{22}A & a_{22}A \end{bmatrix}. \tag{12}$$

To obtain the best parameter sets that describe the *ab initio* band structure, we performed the same fitting approach as described in Sec. IV. We found that, in order to attain the monotonic behavior of the bands, some features of the band structure or the spin splittings are not matched as precisely as the results using the 8×8 Hamiltonian. For instance, the band structures and the spin splittings for InP look reasonable; however, the spin orientation for LH and CH shows opposite trends. For InAs, the spin texture follows the correct behavior; however, the band structure and the spin splittings show the *ab initio* features shifted to higher k values. We show the fitting results for the 6×6 description and the comparison to *ab initio* in the Supplemental Material [76]. The best parameter sets are displayed in Table IV. We would like to emphasize that the

TABLE IV. Parameter sets of the 6×6 valence band Hamiltonian for InAs and InP WZ. The units follow Table III.

Parameter	InAs	InP
Energy splittings		
Δ_1	0.1003	0.0945
Δ_2	0.1038	0.0286
Δ_3	0.1037	0.0310
Linear parameters		
A_7	−0.5565	−0.0917
α_1	−0.0237	0.3309
α_2	−0.0758	−0.0702
α_3	−0.0967	−0.0521
Second order parameters		
A_1	−17.2689	−10.5414
A_2	−1.2047	−1.4542
A_3	16.6637	9.4589
A_4	−7.6202	−3.2741
A_5	−5.9281	3.9468
A_6	−7.3872	−0.2759

most reliable approach is to use the 8×8 Hamiltonian with parameter sets we provide in Sec. IV.

VII. CONCLUSIONS

In this paper, we have calculated the band structure of InAs and InP in the WZ phase using the WIEN2k *ab initio* code. Both compounds have a direct band gap at the Γ point with the SOC effects clearly larger for InAs than InP. Our calculations are consistent with theoretical and experimental reported values in the literature. In order to describe the band structure around the FBZ center, we developed a multiband 8×8 $k \cdot p$ model for the first conduction band and the top three valence bands, including spin. The fitted parameters we obtained for the $k \cdot p$ Hamiltonian recover the important features of the *ab initio* band structure with good agreement up to 1.0 nm^{-1} for multiple directions in the FBZ. Due to the stronger SOC of InAs compared to its crystal field splitting, the labeling of LH and CH energy bands at the Γ point is reversed from InP. Regarding the spin-splitting properties, we included the k-dependent SOC term in the Hamiltonian, which is usually neglected in the literature. This term, combined with the other indirect couplings in the Hamiltonian, allowed the description of the spin-splitting properties farther away from the vicinity of the Γ point. Our model captured all the important features including the description of maxima values and also the crossing between the spin-split bands (clearly seen in the HH band of InP, for instance). All these intricate behaviors of spin splitting have a unique physical origin, the BIA of the WZ structure. Furthermore, we calculated the in-plane spin orientation, i.e., the spin expectation value, of the energy bands and found that they all have a Rashba-like spin texture, either CW or CCW. This spin orientation was also compared to *ab initio* data to correctly identify the signs of the parameters in the Hamiltonian. Using our multiband $k \cdot p$ Hamiltonian, we obtained the DOS for conduction and valence bands and calculated the carrier density as a function of the Fermi energy. In addition to the 8×8 Hamiltonian, we present analytical expressions for the effective masses and the SOC field of conduction band which holds in the vicinities of the Γ point. For completeness, we also fitted the 6×6 $k \cdot p$ model for the valence band to the *ab initio* data. We emphasize that the best effective description that matches our *ab initio* calculations is the full 8×8 $k \cdot p$ Hamiltonian.

In conclusion, we provided in this study robust $k \cdot p$ models and parameter sets that can be straightforwardly applied to investigate novel effects in InAs- and InP-based nanostructures. For instance, polytypic systems of mixed WZ and ZB have already been demonstrated experimentally for both InAs and InP with great growth control of the different phases [2] and there are also theoretical models to treat such systems [10,30,77]. Furthermore, InAs nanowires are also a platform for studies in Majorana fermions [15]. One of the key ingredients for such realization is the presence of a robust SOC to split the energy bands, a feature already included in our model. Finally, it is straightforward to include strain effects by using the well-established WZ strain Hamiltonian [28,30] combined with the elastic constants and deformation potentials for InAs and InP in the WZ phase already reported in the literature [26,78–80].

ACKNOWLEDGMENTS

The authors acknowledge financial support from CAPES PVE (Grant No. 88881.068174/2014-01), CNPq (Grants No. 149904/2013-4, No. 88887.110814/2015-00, and No. 304289/2015-9), DFG SFB 689, and FAPESP (Grant No. 2012/05618-0). P.E.F.J. thanks A. Polimeni for suggesting the calculation of effective masses.

APPENDIX A: EFFECTIVE MASSES

Very close to the Γ point we can estimate the effective masses by fitting a parabolic dispersion to the *ab initio* data. In Table V, we show the values of effective masses along the k_z and k_x directions for the highlighted energy bands of Figs. 2(a) and 2(b). For the k_x direction, we calculated the effective masses assuming the average value of the spin-splitting bands, i.e., $(E_o + E_i)/2$ with the subindex o (i) indicating the outer (inner) branch.

APPENDIX B: HAMILTONIAN TERMS AND PARAMETERS

In this Appendix, we present the matrix forms of all terms in Eq. (5) and the definition of parameters using the simple group formalism.

Matrix representation of H_0:

$$H_0 = \text{diag}[\Delta_1, \Delta_1, 0, \Delta_1, \Delta_1, 0, E_c, E_c], \qquad \text{(B1)}$$

with the definitions $\langle \Gamma_{5v}^x | H_0 | \Gamma_{5v}^x \rangle = \langle \Gamma_{5v}^y | H_0 | \Gamma_{5v}^y \rangle = \Delta_1$, $\langle \Gamma_{1v} | H_0 | \Gamma_{1v} \rangle = 0$, and $\langle \Gamma_{1c} | H_0 | \Gamma_{1c} \rangle = E_c$.

The zero energy is defined without SOC for states $|c_3\rangle$ and $|c_6\rangle$. The parameter Δ_1 is the crystal field splitting energy, which arises due to the WZ anisotropy between the xy plane and z direction, and the conduction band energy is denoted by the parameter E_c. It is possible to make the connection with the energy gap including SOC coupling by writing $E_c = E_g + \Delta_c$, for instance. It is also convenient to consider a diagonal energy offset to set the top valence band at zero energy.

TABLE V. Effective masses for InAs and InP along k_z ($m_\parallel^*$) and k_x ($m_\perp^*$) for the highlighted bands of Figs. 2(a) and 2(b). The effective masses were obtained by fitting a parabola up to 2% of the FBZ along the specified directions.

	InAs		InP	
	$m_\parallel^*$	$m_\perp^*$	$m_\parallel^*$	$m_\perp^*$
Γ_{7c}	0.0370	0.0416	0.0947	0.1183
Γ_{9v}	−0.9738	−0.0795	−1.0646	−0.2091
Γ_{7v}	−0.0551	−0.1046	−0.3064	−0.1988
Γ_{7v}'	−0.0863	−0.1838	−0.1016	−0.4887

Matrix representation of $H_{SO}^{(1)}$:

$$H_{SO}^{(1)} = \begin{bmatrix} \Delta_2 & 0 & 0 & 0 & 0 & 0 & 0 & 0 \\ 0 & -\Delta_2 & 0 & 0 & 0 & \sqrt{2}\Delta_3 & 0 & i\sqrt{2}\Delta_4 \\ 0 & 0 & 0 & 0 & \sqrt{2}\Delta_3 & 0 & 0 & 0 \\ 0 & 0 & 0 & \Delta_2 & 0 & 0 & 0 & 0 \\ 0 & 0 & \sqrt{2}\Delta_3 & 0 & -\Delta_2 & 0 & i\sqrt{2}\Delta_4 & 0 \\ 0 & \sqrt{2}\Delta_3 & 0 & 0 & 0 & 0 & 0 & 0 \\ 0 & 0 & 0 & 0 & -i\sqrt{2}\Delta_4 & 0 & 0 & 0 \\ 0 & -i\sqrt{2}\Delta_4 & 0 & 0 & 0 & 0 & 0 & 0 \end{bmatrix}, \tag{B2}$$

with the definitions

$$\begin{aligned} \Delta_2 &= \frac{i\hbar}{4m_0^2c^2}\langle\Gamma_{5v}^x|\frac{\partial V}{\partial x}p_y - \frac{\partial V}{\partial y}p_x|\Gamma_{5v}^y\rangle, \\ \Delta_3 &= \frac{i\hbar}{4m_0^2c^2}\langle\Gamma_{5v}^y|\frac{\partial V}{\partial y}p_z - \frac{\partial V}{\partial z}p_y|\Gamma_{1v}\rangle = \frac{i\hbar}{4m_0^2c^2}\langle\Gamma_{1v}|\frac{\partial V}{\partial z}p_x - \frac{\partial V}{\partial x}p_z|\Gamma_{5v}^x\rangle, \\ \Delta_4 &= \frac{i\hbar}{4m_0^2c^2}\langle\Gamma_{5v}^y|\frac{\partial V}{\partial y}p_z - \frac{\partial V}{\partial z}p_y|\Gamma_{1c}\rangle = \frac{i\hbar}{4m_0^2c^2}\langle\Gamma_{1c}|\frac{\partial V}{\partial z}p_x - \frac{\partial V}{\partial x}p_z|\Gamma_{5v}^x\rangle. \end{aligned} \tag{B3}$$

Matrix representation of $H_{kp}^{(1)}$:

$$H_{kp}^{(1)} = \begin{bmatrix} 0 & 0 & iA_7k_- & 0 & 0 & 0 & -\frac{1}{\sqrt{2}}P_2k_- & 0 \\ 0 & 0 & -iA_7k_+ & 0 & 0 & 0 & \frac{1}{\sqrt{2}}P_2k_+ & 0 \\ -iA_7k_+ & iA_7k_- & 0 & 0 & 0 & 0 & P_1k_z & 0 \\ 0 & 0 & 0 & 0 & 0 & -iA_7k_+ & 0 & \frac{1}{\sqrt{2}}P_2k_+ \\ 0 & 0 & 0 & 0 & 0 & iA_7k_- & 0 & -\frac{1}{\sqrt{2}}P_2k_- \\ 0 & 0 & 0 & iA_7k_- & -iA_7k_+ & 0 & 0 & P_1k_z \\ -\frac{1}{\sqrt{2}}P_2k_+ & \frac{1}{\sqrt{2}}P_2k_- & P_1k_z & 0 & 0 & 0 & 0 & 0 \\ 0 & 0 & 0 & \frac{1}{\sqrt{2}}P_2k_- & -\frac{1}{\sqrt{2}}P_2k_+ & P_1k_z & 0 & 0 \end{bmatrix}, \tag{B4}$$

with the definitions

$$\begin{aligned} A_7 &= \frac{i}{\sqrt{2}}\frac{\hbar}{m_0}\langle\Gamma_{5v}^x|p_x|\Gamma_{1v}\rangle = \frac{i}{\sqrt{2}}\frac{\hbar}{m_0}\langle\Gamma_{5v}^y|p_y|\Gamma_{1v}\rangle, \\ P_2 &= i\frac{\hbar}{m_0}\langle\Gamma_{5v}^x|p_x|\Gamma_{1c}\rangle = i\frac{\hbar}{m_0}\langle\Gamma_{5v}^y|p_y|\Gamma_{1c}\rangle, \\ P_1 &= i\frac{\hbar}{m_0}\langle\Gamma_{1v}|p_z|\Gamma_{1c}\rangle, \\ k_\pm &= k_x \pm ik_y. \end{aligned} \tag{B5}$$

Matrix representation of $H_{kSO}^{(1)}$:

$$H_{kSO}^{(1)} = \begin{bmatrix} 0 & 0 & -\frac{i}{\sqrt{2}}\alpha_1k_- & 0 & -i\alpha_2k_- & 0 & \frac{1}{\sqrt{2}}\beta_1k_- & 0 \\ 0 & 0 & -\frac{i}{\sqrt{2}}\alpha_1k_+ & -i\alpha_2k_- & 0 & i\sqrt{2}\alpha_1k_z & \frac{1}{\sqrt{2}}\beta_1k_+ & -\sqrt{2}\beta_1k_z \\ \frac{i}{\sqrt{2}}\alpha_1k_+ & \frac{i}{\sqrt{2}}\alpha_1k_- & 0 & 0 & -i\sqrt{2}\alpha_1k_z & -i\alpha_3k_- & 0 & \beta_2k_- \\ 0 & i\alpha_2k_+ & 0 & 0 & 0 & \frac{i}{\sqrt{2}}\alpha_1k_+ & 0 & -\frac{1}{\sqrt{2}}\beta_1k_+ \\ i\alpha_2k_+ & 0 & i\sqrt{2}\alpha_1k_z & 0 & 0 & \frac{i}{\sqrt{2}}\alpha_1k_- & -\sqrt{2}\beta_1k_z & -\frac{1}{\sqrt{2}}\beta_1k_- \\ 0 & -i\sqrt{2}\alpha_1k_z & i\alpha_3k_+ & -\frac{i}{\sqrt{2}}\alpha_1k_- & -\frac{i}{\sqrt{2}}\alpha_1k_+ & 0 & -\beta_2k_+ & 0 \\ \frac{1}{\sqrt{2}}\beta_1k_+ & \frac{1}{\sqrt{2}}\beta_1k_- & 0 & 0 & -\sqrt{2}\beta_1k_z & -\beta_2k_- & 0 & -i\gamma_1k_- \\ 0 & -\sqrt{2}\beta_1k_z & \beta_2k_+ & -\frac{1}{\sqrt{2}}\beta_1k_- & -\frac{1}{\sqrt{2}}\beta_1k_+ & 0 & i\gamma_1k_+ & 0 \end{bmatrix}, \tag{B6}$$

with the definitions

$$\begin{aligned}
\alpha_1 &= \frac{\hbar^2}{4m_0^2c^2}\langle\Gamma_{5v}^x|\frac{\partial V}{\partial x}|\Gamma_{1v}\rangle = \frac{\hbar^2}{4m_0^2c^2}\langle\Gamma_{5v}^y|\frac{\partial V}{\partial y}|\Gamma_{1v}\rangle,\\
\alpha_2 &= \frac{\hbar^2}{4m_0^2c^2}\langle\Gamma_{5v}^x|\frac{\partial V}{\partial z}|\Gamma_{5v}^x\rangle = \frac{\hbar^2}{4m_0^2c^2}\langle\Gamma_{5v}^y|\frac{\partial V}{\partial z}|\Gamma_{5v}^y\rangle,\\
\alpha_3 &= \frac{\hbar^2}{4m_0^2c^2}\langle\Gamma_{1v}|\frac{\partial V}{\partial z}|\Gamma_{1v}\rangle,\\
\beta_1 &= \frac{\hbar^2}{4m_0^2c^2}\langle\Gamma_{5v}^x|\frac{\partial V}{\partial x}|\Gamma_{1c}\rangle = \frac{\hbar^2}{4m_0^2c^2}\langle\Gamma_{5v}^y|\frac{\partial V}{\partial y}|\Gamma_{1c}\rangle,\\
\beta_2 &= \frac{\hbar^2}{4m_0^2c^2}\langle\Gamma_{1v}|\frac{\partial V}{\partial z}|\Gamma_{1c}\rangle,\\
\gamma_1 &= \frac{\hbar^2}{4m_0^2c^2}\langle\Gamma_{1c}|\frac{\partial V}{\partial z}|\Gamma_{1c}\rangle.
\end{aligned} \tag{B7}$$

Matrix representation of $H_{kp}^{(2)}$:

$$H_{kp}^{(2)} = \begin{bmatrix}
\lambda+\theta & -K^* & -H^* & 0 & 0 & 0 & T^* & 0\\
-K & \lambda+\theta & H & 0 & 0 & 0 & T & 0\\
-H & H^* & \lambda & 0 & 0 & 0 & U & 0\\
0 & 0 & 0 & \lambda+\theta & -K & H & 0 & T\\
0 & 0 & 0 & -K^* & \lambda+\theta & -H^* & 0 & T^*\\
0 & 0 & 0 & H^* & -H & \lambda & 0 & U\\
T & T^* & U^* & 0 & 0 & 0 & V & 0\\
0 & 0 & 0 & T^* & T & U^* & 0 & V
\end{bmatrix}, \tag{B8}$$

with elements given by

$$\begin{aligned}
\lambda &= A_1k_z^2 + A_2\big(k_x^2 + k_y^2\big),\\
\theta &= A_3k_z^2 + A_4\big(k_x^2 + k_y^2\big),\\
K &= A_5k_+^2,\\
H &= A_6k_+k_z,\\
T &= iB_3k_+k_z,\\
U &= i\big[B_1k_z^2 + B_2\big(k_x^2 + k_y^2\big)\big],\\
V &= e_1k_z^2 + e_2\big(k_x^2 + k_y^2\big),
\end{aligned} \tag{B9}$$

and all the parameters in units of $\hbar^2/2m_0$.

The term $\mathbf{H_{k2}}$ is already included in the diagonal terms of $H_{kp}^{(2)}$. Strictly speaking, the matrix representation $H_{kp}^{(2)}$ is defined as

$$H^{(2)}_{kp,\alpha\alpha'} = \mathbf{H_{k2}}\delta_{\alpha\alpha'} + \sum_{\beta}^{B}\frac{\langle\alpha|\mathbf{H_{kp}}|\beta\rangle\langle\beta|\mathbf{H_{kp}}|\alpha'\rangle}{E_{\alpha\alpha'} - E_\beta}. \tag{B10}$$

The second-order $k \cdot p$ parameters A_1 to A_6 are defined the same way as in Ref. [28], while e_1, e_2, B_1, B_2, and B_3 are given by

$$\begin{aligned}
e_1 &= 1 + \frac{2}{m_0}\sum_{\beta}^{B[\Gamma_1]}\frac{|\langle\Gamma_{1c}|p_z|\beta\rangle|^2}{E_{1c} - E_\beta},\\
e_2 &= 1 + \frac{2}{m_0}\sum_{\beta}^{B[\Gamma_5]}\frac{|\langle\Gamma_{1c}|p_x|\beta\rangle|^2}{E_{1c} - E_\beta}\\
&= 1 + \frac{2}{m_0}\sum_{\beta}^{B[\Gamma_5]}\frac{|\langle\Gamma_{1c}|p_y|\beta\rangle|^2}{E_{1c} - E_\beta},\\
B_1 &= \frac{2}{m_0}\sum_{\beta}^{B[\Gamma_1]}\frac{\langle\Gamma_{1v}|p_z|\beta\rangle\langle\beta|p_z|\Gamma_{1c}\rangle}{E_{1v1c} - E_\beta},\\
B_2 &= \frac{2}{m_0}\sum_{\beta}^{B[\Gamma_5]}\frac{\langle\Gamma_{1v}|p_x|\beta\rangle\langle\beta|p_x|\Gamma_{1c}\rangle}{E_{1v1c} - E_\beta}\\
&= \frac{2}{m_0}\sum_{\beta}^{B[\Gamma_5]}\frac{\langle\Gamma_{1v}|p_y|\beta\rangle\langle\beta|p_y|\Gamma_{1c}\rangle}{E_{1v1c} - E_\beta},\\
B_3 &= \frac{\sqrt{2}}{m_0}\left(\sum_{\beta}^{B[\Gamma_1]}\frac{\langle\Gamma_{5v}^x|p_x|\beta\rangle\langle\beta|p_z|\Gamma_{1c}\rangle}{E_{5v1c} - E_\beta}\right.\\
&\quad\left. + \sum_{\beta}^{B[\Gamma_5]}\frac{\langle\Gamma_{5v}^x|p_z|\beta\rangle\langle\beta|p_x|\Gamma_{1c}\rangle}{E_{5v1c} - E_\beta}\right)\\
&= \frac{\sqrt{2}}{m_0}\left(\sum_{\beta}^{B[\Gamma_1]}\frac{\langle\Gamma_{5v}^y|p_y|\beta\rangle\langle\beta|p_z|\Gamma_{1c}\rangle}{E_{5v1c} - E_\beta}\right.\\
&\quad\left. + \sum_{\beta}^{B[\Gamma_5]}\frac{\langle\Gamma_{5v}^y|p_z|\beta\rangle\langle\beta|p_y|\Gamma_{1c}\rangle}{E_{5v1c} - E_\beta}\right),
\end{aligned} \tag{B11}$$

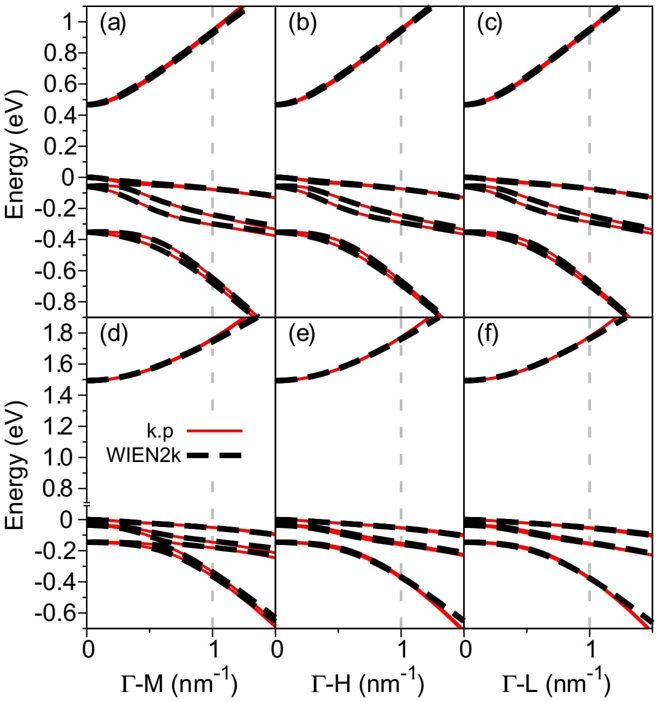

FIG. 8. Comparison of band structures for (a) Γ-M, (b) Γ-H, and (c) Γ-L directions of InAs and (d) Γ-M, (e) Γ-H, and (f) Γ-L directions of InP. The line schemes follow Fig. 4.

with nonzero contributions represented by the irreducible representations in the brackets above the summation.

APPENDIX C: FITTING IN OTHER DIRECTIONS

The comparison between the fitted and WIEN2k *ab initio* band structures is displayed in Fig. 8 for the Γ-M, Γ-H, and Γ-L directions. For the Γ-M direction, we have the same behavior discussed for Γ-K. However, the $k \cdot p$ band structures in the Γ-H and Γ-L directions have closer values to *ab initio*. This better agreement arises from the second-order parameters A_6 and B_3 which only couple the $k_x k_y$ plane to k_z, providing additional corrections to the band structures.

In Fig. 9 and Fig. 10, we show the comparison of spin splittings along the Γ-M, Γ-H, and Γ-L directions for InAs and InP, respectively. For the Γ-H and Γ-L directions, the spin splittings are usually smaller compared to Γ-K and Γ-M. This difference, however, depends on the material and the energy band. For instance, CH and LH values for InAs in Γ-H and Γ-L are approximately half the value in the Γ-K and Γ-M directions while LH and CH values for InP are approximately one-fourth of the values. Because of these larger differences for InP, the spin splittings for CH bands along Γ-H and Γ-L show a small deviation compared to *ab initio* [Figs. 10(h) and 10(l)]. However, the crossings for HH bands [Figs. 10(f) and 10(j)] are precisely reproduced. Comparing all directions, we verify that our $k \cdot p$ model and parameter sets reproduce with great agreement the *ab initio* band structure and spin splittings along all the considered directions of the FBZ.

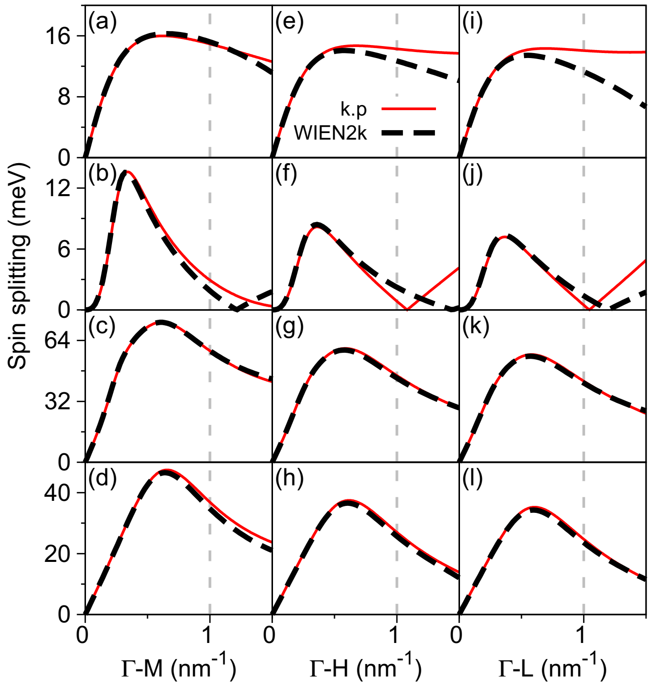

FIG. 9. Comparison of the InAs spin splittings for (a), (e), (i) CB; (b), (f), (j) HH; (c), (g), (k) CH; and (d), (h), (l) LH along Γ-M, Γ-H, and Γ-L directions. The line schemes follow Fig. 4.

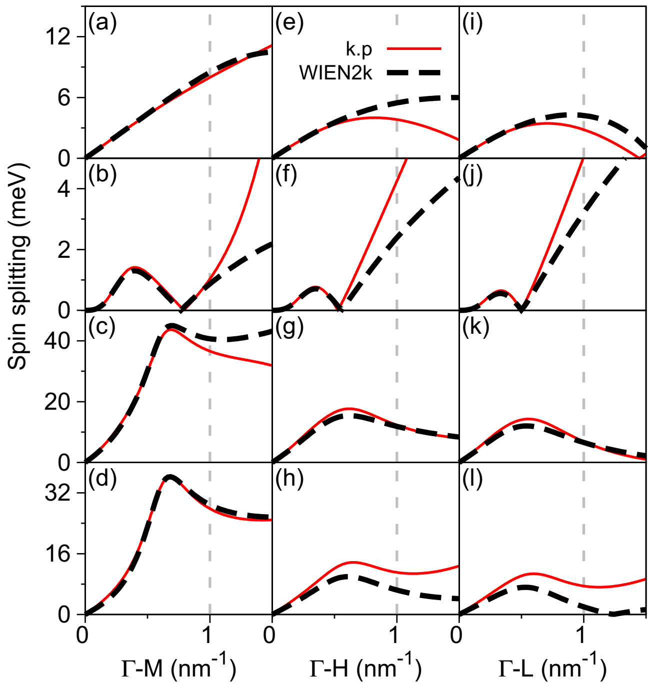

FIG. 10. Comparison of the InP spin splittings for (a), (e), (i) CB; (b), (f), (j) HH; (c), (g), (k) LH; and (d), (h), (l) CH along Γ-M, Γ-H, and Γ-L directions. The line schemes follow Fig. 4.

[1] Y. Li, F. Qian, J. Xiang, and C. M. Lieber, Mater. Today **9**, 18 (2006).
[2] P. Caroff, K. A. Dick, J. Johansson, M. E. Messing, K. Deppert, and L. Samuelson, Nat. Nanotechnol. **4**, 50 (2009).
[3] T. T. T. Vu, T. Zehender, M. A. Verheijen, S. R. Plissard, G. W. G. Immink, J. E. M. Haverkort, and E. P. A. M. Bakkers, Nanotechnology **24**, 115705 (2013).
[4] D. Pan, M. Fu, X. Yu, X. Wang, L. Zhu, S. Nie, S. Wang, Q. Chen, P. Xiong, S. von Molnár, and J. Zhao, Nano Lett. **14**, 1214 (2014).
[5] K. A. Dick, C. Thelander, L. Samuelson, and P. Caroff, Nano Lett. **10**, 3494 (2010).
[6] J. Bolinsson, P. Caroff, B. Mandl, and K. A. Dick, Nanotechnology **22**, 265606 (2011).
[7] S. Lehmann, J. Wallentin, D. Jacobsson, K. Deppert, and K. A. Dick, Nano Lett. **13**, 4099 (2013).
[8] T. Ba Hoang, A. F. Moses, L. Ahtapodov, H. Zhou, D. L. Dheeraj, A. T. J. van Helvoort, B.-O. Fimland, and H. Weman, Nano Lett. **10**, 2927 (2010).
[9] E. G. Gadret, G. O. Dias, L. C. O. Dacal, M. M. de Lima, C. V. R. S. Ruffo, F. Iikawa, M. J. S. P. Brasil, T. Chiaramonte, M. A. Cotta, L. H. G. Tizei, D. Ugarte, and A. Cantarero, Phys. Rev. B **82**, 125327 (2010).
[10] P. E. Faria Junior, T. Campos, and G. M. Sipahi, J. Appl. Phys. **116**, 193501 (2014).
[11] C. Thelander, P. Caroff, S. Plissard, A. Dey, and K. Dick, Nano Lett. **11**, 2424 (2011).
[12] A. Konar, J. Mathew, K. Nayak, M. Bajaj, R. K. Pandey, S. Dhara, K. V. R. M. Murali, and M. M. Deshmukh, Nano Lett. **15**, 1684 (2015).
[13] J. Li, X. Yan, F. Sun, X. Zhang, and X. Ren, Appl. Phys. Lett. **107**, 263103 (2015).
[14] P. Chuang, S.-C. Ho, L. W. Smith, F. Sfigakis, M. Pepper, C.-H. Chen, J.-C. Fan, J. P. Griffiths, I. Farrer, H. E. Beere, G. A. C. Jones, D. A. Ritchie, and T.-M. Chen, Nat. Nanotechnol. **10**, 35 (2014).
[15] A. Das, Y. Ronen, Y. Most, Y. Oreg, M. Heiblum, and H. Shtrikman, Nat. Phys. **8**, 887 (2012).
[16] X. Li, X. Wei, T. Xu, D. Pan, J. Zhao, and Q. Chen, Adv. Mater. **27**, 2852 (2015).
[17] H. J. Joyce, C. J. Docherty, Q. Gao, H. H. Tan, C. Jagadish, J. Lloyd-Hughes, L. M. Herz, and M. B. Johnston, Nanotechnology **24**, 214006 (2013).
[18] Y. Cui, J. Wang, S. R. Plissard, A. Cavalli, T. T. T. Vu, R. P. J. van Veldhoven, L. Gao, M. Trainor, M. A. Verheijen, J. E. M. Haverkort, and E. P. A. M. Bakkers, Nano Lett. **13**, 4113 (2013).
[19] Z. Wang, B. Tian, M. Paladugu, M. Pantouvaki, N. Le Thomas, C. Merckling, W. Guo, J. Dekoster, J. V. Campenhout, P. Absil, and D. V. Thourhout, Nano Lett. **13**, 5063 (2013).
[20] S. F. Svensson, S. Jeppesen, C. Thelander, L. Samuelson, H. Linke, and K. A. Dick, Nanotechnology **24**, 345601 (2013).
[21] D. Lindgren, K. Kawaguchi, M. Heurlin, M. T. Borgström, M.-E. Pistol, L. Samuelson, and A. Gustafsson, Nanotechnology **24**, 225203 (2013).
[22] Z. Zanolli, F. Fuchs, J. Furthmüller, U. von Barth, and F. Bechstedt, Phys. Rev. B **75**, 245121 (2007).
[23] A. De and C. E. Pryor, Phys. Rev. B **81**, 155210 (2010).
[24] L. C. O. Dacal and A. Cantarero, Solid State Commun. **151**, 781 (2011).
[25] A. Belabbes, C. Panse, J. Furthmüller, and F. Bechstedt, Phys. Rev. B **86**, 075208 (2012).
[26] C. Hajlaoui, L. Pedesseau, F. Raouafi, F. Ben CheikhLarbi, J. Even, and J.-M. Jancu, J. Phys. D: Appl. Phys. **46**, 505106 (2013).
[27] L. C. O. Dacal and A. Cantarero, Mater. Res. Express **1**, 015702 (2014).
[28] S. L. Chuang and C. S. Chang, Phys. Rev. B **54**, 2491 (1996).
[29] P. Rinke, M. Winkelnkemper, A. Qteish, D. Bimberg, J. Neugebauer, and M. Scheffler, Phys. Rev. B **77**, 075202 (2008).
[30] P. E. Faria Junior and G. M. Sipahi, J. Appl. Phys. **112**, 103716 (2012).
[31] T. Cheiwchanchamnangij and W. R. Lambrecht, Phys. Rev. B **84**, 035203 (2011).
[32] P. Blaha, K. Schwarz, G. K. H. Madsen, D. Kvasnicka, and J. Luitz, *WIEN2k, An Augmented Plane Wave + Local Orbitals Program for Calculating Crystal Properties* (Vienna University of Technology, Vienna, 2013).
[33] I. Žutić, J. Fabian, and S. Das Sarma, Rev. Mod. Phys. **76**, 323 (2004).
[34] J. Hohenberg and W. Kohn, Phys. Rev. **136**, B864 (1964).
[35] A. D. Becke and E. R. Johnson, J. Chem. Phys. **124**, 221101 (2006).
[36] F. Tran and P. Blaha, Phys. Rev. Lett. **102**, 226401 (2009).
[37] Y.-S. Kim, M. Marsman, G. Kresse, F. Tran, and P. Blaha, Phys. Rev. B **82**, 205212 (2010).
[38] D. Koller, F. Tran, and P. Blaha, Phys. Rev. B **83**, 195134 (2011).
[39] D. Koller, F. Tran, and P. Blaha, Phys. Rev. B **85**, 155109 (2012).
[40] Y.-S. Kim, K. Hummer, and G. Kresse, Phys. Rev. B **80**, 035203 (2009).
[41] A. N. Chantis, M. van Schilfgaarde, and T. Kotani, Phys. Rev. Lett. **96**, 086405 (2006).
[42] J.-W. Luo, G. Bester, and A. Zunger, Phys. Rev. Lett. **102**, 056405 (2009).
[43] A. N. Chantis, N. E. Christensen, A. Svane, and M. Cardona, Phys. Rev. B **81**, 205205 (2010).
[44] J. P. Perdew and A. Zunger, Phys. Rev. B **23**, 5048 (1981).
[45] J. P. Perdew, K. Burke, and M. Ernzerhof, Phys. Rev. Lett. **77**, 3865 (1996).
[46] D. J. Singh and L. Nordstrom, *Planewaves, Pseudopotentials, and the LAPW Method* (Springer, Berlin, 2006).
[47] M. Gmitra and J. Fabian, arXiv:1606.00588.
[48] M. S. Dresselhaus, G. Dresselhaus, and A. Jorio, *Group Theory: Application to the Physics of Condensed Matter*, 1st ed. (Springer, Berlin, 2008). From Table D.11, replace $\Delta_{1\dots6}$ with $\Gamma_{1\dots6}$ and use the factor $T_\Delta = 1$.
[49] M. Cardona, N. E. Christensen, and G. Fasol, Phys. Rev. B **38**, 1806 (1988).
[50] P. Käckell, B. Wenzien, and F. Bechstedt, Phys. Rev. B **50**, 17037 (1994).
[51] M. I. McMahon and R. J. Nelmes, Phys. Rev. Lett. **95**, 215505 (2005).
[52] D. Kriegner, C. Panse, B. Mandl, K. A. Dick, M. Keplinger, J. M. Persson, P. Caroff, D. Ercolani, L. Sorba, F. Bechstedt, J. Stangl, and G. Bauer, Nano Lett. **11**, 1483 (2011).
[53] C. Panse, D. Kriegner, and F. Bechstedt, Phys. Rev. B **84**, 075217 (2011).
[54] R. C. Casella, Phys. Rev. **114**, 1514 (1959).
[55] J. J. Hopfield, J. Appl. Phys. **32**, 2277 (1961).

[56] M. De Luca, A. Zilli, A. Fonseka, S. Mokkapati, A. Miriametro, H. Tan, L. Smith, C. Jagadish, M. Capizzi, and A. Polimeni, Nano Lett. **15**, 998 (2015).

[57] A. Zilli, M. De Luca, D. Tedeschi, A. Fonseka, A. Miriametro, H. Tan, C. Jagadish, M. Capizzi, and A. Polimeni, ACS Nano **9**, 4277 (2015).

[58] R. Enderlein and N. J. Horing, *Fundamentals of Semiconductor Physics and Devices*, 1st ed. (World Scientific Publishing, Singapore, 1997).

[59] P. O. Löwdin, J. Chem. Phys. **19**, 1396 (1951).

[60] J. Bao, D. C. Bell, F. Capasso, N. Erdman, D. Wei, L. Fröberg, T. Mårtensson, and L. Samuelson, Adv. Mater. **21**, 3654 (2009).

[61] G. Koblmüller, S. Hertenberger, K. Vizbaras, M. Bichler, F. Bao, J-P. Zhang, and G. Abstreiter, Nanotechnology **21**, 365602 (2010).

[62] M. Möller, M. M. de Lima Jr., A. Cantarero, T. Chiaramonte, M. A. Cotta, and F. Iikawa, Nanotechnology **23**, 375704 (2012).

[63] A. Mishra, L. V. Titova, T. B. Hoang, H. E. Jackson, L. M. Smith, J. M. Yarrison-Rice, Y. Kim, H. J. Joyce, Q. Gao, H. H. Tan, and C. Jagadish, Appl. Phys. Lett. **91**, 263104 (2007).

[64] G. L. Tuin, M. T. Borgström, J. Trägårdh, M. Ek, L. R. Wallenberg, L. Samuelson, and M.-E. Pistol, Nano Res. **4**, 159 (2011).

[65] As far as we are concerned, the only paper in the literature that provides a double-group description of the $k \cdot p$ model (for cubic crystals) is W. J. Elder, R. M. Ward, and J. Zhang, Phys. Rev. B **83**, 165210 (2011).

[66] Explicitly, $u_{n,\Gamma}(\vec{r}) = \langle \vec{r} | c_n \rangle$, with $n = 1, \ldots, 8$ running over the energy bands at the Γ point we are describing.

[67] R. Beresford, J. Appl. Phys. **95**, 6216 (2004).

[68] J. Y. Fu and M. W. Wu, J. Appl. Phys. **104**, 093712 (2008).

[69] A. Marnetto, M. Penna, and M. Goano, J. Appl. Phys. **108**, 033701 (2010).

[70] M. S. Miao, Q. Yan, C. G. Van de Walle, W. K. Lou, L. L. Li, and K. Chang, Phys. Rev. Lett. **109**, 186803 (2012).

[71] G. Dresselhaus, Phys. Rev. **100**, 580 (1955).

[72] A. Punya and W. R. L. Lambrecht, Phys. Rev. B **85**, 195147 (2012).

[73] M. Newville, T. Stensitzki, D. B. Allen, and A. Ingargiola, LMFIT: Non-linear least-square minimization and curve-fitting for Python (2014), doi:10.5281/zenodo.11813.

[74] The residue calculated for a specific direction in the FBZ is given by $r = \frac{1}{N} \sum_{n,\vec{k}} [f_n(\vec{k}) - t_n(\vec{k})]^2$, in which n runs over the 8 energy bands or 4 spin splitting curves, $\vec{k}$ runs over the k points, $f_n(\vec{k})$ is the fitted data, $t_n(\vec{k})$ is the *ab initio* data, and N is a normalization constant which includes the number of k points used multiplied by the size of n. The total residue is the sum of the residues in all directions.

[75] S. L. Chuang and C. S. Chang, Appl. Phys. Lett. **68**, 1657 (1996).

[76] See Supplemental Material at http://link.aps.org/supplemental/10.1103/PhysRevB.93.235204 for the curve fitting of the carrier density, the comparison between *ab initio* and the analytical approach for conduction band and the fitting of the 6×6 Hamiltonian approach for valence band.

[77] J. I. Climente, C. Segarra, F. Rajadell, and J. Planelles, J. Appl. Phys. **119**, 125705 (2016).

[78] M. W. Larsson, J. B. Wagner, M. Wallin, P. Håkansson, L. E. Fröberg, L. Samuelson, and L. R. Wallenberg, Nanotechnology **18**, 015504 (2007).

[79] F. Boxberg, N. Søndergaard, and H. Q. Xu, Adv. Mater. **24**, 4692 (2012).

[80] C. Hajlaoui, L. Pedesseau, F. Raouafi, F. Ben Cheikh Larbi, J. Even, and J.-M. Jancu, J. Exp. Theor. Phys. **121**, 246 (2015).